Numerical and laboratory attoclock simulations on noble-gas atoms

Vladislav V. Serov,[1] Joshua Cesca,[2] and Anatoli S. Kheifets[2]
[1]*Department of Theoretical Physics, Saratov State University, 83 Astrakhanskaya, Saratov 410012, Russia*
[2]*Research School of Physics, The Australian National University, Canberra ACT 2601, Australia*

(Received 17 December 2020; accepted 1 February 2021; published 16 February 2021)

We conduct a systematic theoretical study of strong field tunneling ionization of noble-gas atoms, from He to Kr, by elliptically polarized laser pulses in the so-called attoclock setup. Our theoretical model is based on a numerical solution of the time-dependent Schrödinger equation in the single active electron approximation. We simulate laboratory measurements utilizing few optical cycle pulses to benchmark our calculations against experiment. We further conduct "numerical attoclock" simulations with short, nearly single-cycle pulses to test various tunneling ionization models. We examine the attoclock offset angles as affected by the target orbital structure and the laser pulse intensity. Finally, we exclude a finite tunneling time scenario and attribute the attoclock offset angle entirely to the Coulomb field of the ion remainder as was recently demonstrated for the hydrogen atom [U. S. Sainadh *et al.*, Nature (London) **568**, 75 (2019)].

DOI: 10.1103/PhysRevA.103.023110

I. INTRODUCTION

Tunneling ionization of noble-gas atoms by circularly or elliptically polarized laser pulses has been studied actively over the past decade. It has been suggested that the photoelectron momentum distribution (PMD) following such an ionization process can be used for mapping orbital structure of the target [1]. The use of circularly polarized light rather than linear polarization minimizes rescattering and intercycle interference to produce two-dimensional PMD images with a clear signature of the angular orbital structure [2]. Electron momentum imaging with circular or elliptical light can also be employed for testing various tunneling ionization scenarios [3,4]. Another major use of PMDs with elliptical polarization is the so-called attoclock setup aiming to resolve the tunneling time that a photoelectron spends under the barrier [5–7]. "Improved" attoclocks driven by two laser pulses (double-handed attoclocks) have also been proposed [8,9]. Results of earlier and more recent measurements of tunneling time in noble-gas atoms [10–12] are a subject of the continuing debate [13,14]. Meanwhile, the cleanest attoclock measurement on the atomic hydrogen has effectively eliminated a finite tunneling time scenario [15]. Another interesting effect discovered in tunneling ionization of noble-gas atoms with circular light is its strong dependence on the angular momentum projection of the target orbital [16]. It appears that ionization with a light wave counter-rotating with the electron cloud has a strong propensity over the corotating one. This effect can be used to produce nearly complete spin polarization of the photoelectron beam [17,18]. Such a strong angular momentum dependence can also be observed in the Wigner time delay [19] and the attoclock offset angles [20–22].

Despite this rich physics that can be probed by attoclock experiments on noble-gas atoms, only very few measurements have been reported to date on heavier atoms beyond helium [7,9,12]. This makes a compelling motivation for a systematic attoclock investigation across a series of target atoms in a wide range of field intensities. Such experimental investigation is currently underway [23]. To guide this investigation, we conduct a systematic theoretical study of tunneling ionization of noble-gas atoms, from He to Kr, in the attoclock setup. In our modeling, we simulate experimental parameters similar to those employed previously in the atomic hydrogen measurement [15]. We study PMD projected on the polarization plane of a close to circular (ellipticity $\epsilon = 0.84$) laser light with the pulse duration of several optical cylces (FWHM = 6.8 fs at 770 nm). We model this process by solving the time-dependent Schrödinger equation (TDSE) in the single active electron (SAE) approximation. Beyond the SAE and the usage of a localized numerical one-electron potential, our theoretical approach is free from any further approximations and thus it provides an accurate nonperturbative description of electron ionization dynamics. We simulate the experimental PMD and observe a close resemblance between the measured and simulated electron momentum distributions. Because of our usage of multicycle laser pulses, the simulated PMD's have complex structure with a manifold of concentric above threshold ionization (ATI) rings. These rings are blurred in the experiment because of the focus volume averaging effect. In theory, each ATI ring has its angular maximum shifted slightly relative to its neighbors [24]. Radial momentum integration over the ATI structure results in an angular distribution which deviates from a simple Gaussian shape that makes an accurate determination of the attoclock offset angle less straightforward. In comparison, the PMD with very short, circular polarized, nearly single-cycle pulses is much simpler. In this case, the attoclock offset angle can be uniquely and accurately identified. Even though these short pulses cannot be readily deployed in laboratory studies, such "numerical attoclock" simulations are very informative and can be used

for testing and verification of various tunneling ionization scenarios [25–29]. In this work, we also conduct numerical attoclock simulations on noble-gas atoms and investigate the orbital structure effect on the magnitude of the PMD and the attoclock offset angle. The former effect is explained within the semiclassical saddle-point method (SPM) [16,30]. To explain the latter effect, we employ the classical Keldysh-Rutherford (KR) model [28] and relate a strong dependence of this angle on the angular momentum projection of the target orbital with the velocity of the photoelectron exiting the tunnel. Finally, we modify the one-electron potential by reducing the asymptotic charge of the ion remainder while keeping the inner part of this potential intact. The attoclock offset angle in such a modified potential becomes very close to zero. This effectively excludes a finite tunneling time scenario and attributes the attoclock offset angle entirely to the Coulomb field of the ion remainder as was recently shown for the hydrogen atom [15].

The rest of the paper is organized into the following sections. In Sec. II A we outline our computational techniques and in Sec. II B we present our semiclassical and classical models. In Sec. III we discuss and interpret our main numerical and analytical findings. Finally, we conclude in Sec. IV by outlining further possible extensions of this study.

II. THEORETICAL MODELING

A. Numerical techniques

We solve numerically the TDSE

$$i\partial\Psi(\boldsymbol{r},t)/\partial t = [\hat{H}_{\rm atom} + \hat{H}_{\rm int}(t)]\Psi(\boldsymbol{r},t), \tag{1}$$

where $\hat{H}_{\rm atom}$ describes a field-free atom and contains a localized one-electron potential. The interaction Hamiltonian is written in the velocity gauge

$$\hat{H}_{\rm int}(t) = \boldsymbol{A}(t)\cdot\hat{\boldsymbol{p}}, \quad \boldsymbol{E}(t) = -\partial\boldsymbol{A}/\partial t. \tag{2}$$

Here and throughout, the atomic system of units is in use such that $e = m = \hbar = 1$. The vector potential in Eq. (2) is defined by the following expression:

$$\boldsymbol{A}(t) = \frac{A_0}{\sqrt{\epsilon^2+1}}\cos^4\left(\frac{\omega t}{2N}\right)\begin{bmatrix}\epsilon\,\cos(\omega t+\phi)\,\boldsymbol{e}_x\\ \sin(\omega t+\phi)\,\boldsymbol{e}_y\end{bmatrix}. \tag{3}$$

Here, we introduce the ellipticity parameter ϵ, the angular frequency ω, and the carrier envelope phase (CEP) ϕ. The pulse length is parametrized with the number of optical cycles N and the envelope function $f(t)$ vanishes for $|t| \geqslant N\pi/\omega$. The (mean) field intensity is given by $I = (\omega A_0)^2$ and the frequency ω is taken to correspond to 770 nm wavelength. The multicycle pulses with $\epsilon = 0.84$, $N = 5$, and $\phi = 0, \pi$ were employed to model the ongoing experiment [23]. As in this experiment, the field intensity was fixed for each atom and incremented from the heaviest Kr to the lightest He to compensate for the increasing ionization potential I_p and to keep the corresponding tunnel width I_p/E approximately constant. A selection of the fixed intensities is shown in Table I. For numerical attoclock simulations, the single-oscillation pulses at 800 nm were employed by selecting $\epsilon = 1$, $N = 2$, and $\phi = 0$ as in [29]. Because the numerical attoclock simulations are much less time consuming, a wide range of the field intensities were spanned for each of the target atoms.

TABLE I. The laser pulse intensity I (in units of 10^{14} W/cm^2) selected for laboratory attoclock simulations on various target atoms as guided by the ionization potential I_p (shown in Rydbergs). The corresponding Keldysh parameters γ are also displayed.

Atom	I_p (Ry)	I, $10^{14}\times$ W/cm^2	γ
He	1.81	4.0	0.75
Ne	1.59	3.6	0.71
Ar	1.16	3.0	0.69
Kr	1.03	2.65	0.69
H	1	2.5	0.70

The TDSE (1) was solved by two different numerical techniques: the spherical-coordinate implicit derivatives (method) (SCID)-TDSE [31] and the split-operator method (SOM) [32]. To extract the ionization amplitudes from the calculated wave function without the explicit boundary conditions, two different methods were also used: the ISURF method [33] and the t-SURFFC method [34], respectively. Both methods belong to the family of the time-dependent surface flux methods (t-SURFF).

The SCID-TDSE/ISURF method was used previously for the hydrogen attoclock simulations [15]. Both SCID-TDSE/ISURF and SOM/t-SURFFC methods were employed for numerical attoclock simulations [29]. The two TDSE codes [32,33] were benchmarked against each other and their results were found to be very close.

The solution of TDSE (1) was sought with the initial condition $\Psi_{nlm}(\boldsymbol{r}, t = -\pi N/\omega) = \psi_{nlm}(\boldsymbol{r})$, where the set of quantum numbers n, l, m defines the bound target orbital. The photoelectron momentum distribution for the given initial state is

$$P_m(\boldsymbol{k}) = |\langle\varphi_{\boldsymbol{k}}(r)|\Psi_{nlm}(\boldsymbol{r}, t\to\infty)|\rangle|^2. \tag{4}$$

Here, the indices n, l are dropped on the left for brevity of notations. Because of an exponential decrease of the ionization probability with an increasing binding energy, the dominant contribution to the PMD (4) comes from the outermost atomic shell. In the present case, it is the np valence shell of a noble-gas atom. In attoclock measurements, the experimentally observed quantity is the PMD (4) projected on the polarization (x, y) plane and summed over the unresolved initial state angular momentum projections:

$$\overline{P}(k_x, k_y) = \int_{-\infty}^{\infty} dk_z \sum_m P_m(\boldsymbol{k}). \tag{5}$$

We also analyze partially integrated PMDs in the form of the photoelectron energy spectrum collected from all the emission directions:

$$P_m(E) = \int k\, d\Omega_k P_m(\boldsymbol{k}), \quad E = k^2/2. \tag{6}$$

Another integral quantity that we analyze is the angular profile

$$P_m(\theta) = \int k\, dk\, \bar{P}_m(k_x, k_y),$$
$$k = \left(k_x^2 + k_y^2\right)^{1/2}, \quad \theta = \tan^{-1}(k_y/k_x). \tag{7}$$

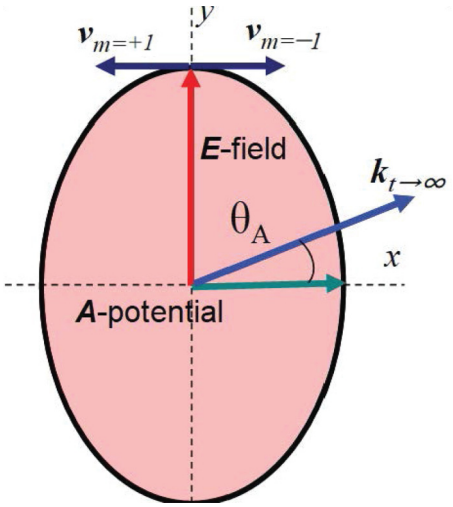

FIG. 1. Polarization ellipse of the laser field. The electric field $\boldsymbol{E}(t_0)$ along $\hat{y}$ defines the direction of tunneling and the tunneling width y_0. The initial velocity in this direction v_{yi} in (12) is purely imaginary. The vector potential $\boldsymbol{A}(t_0)$ along $\hat{x}$ defines the photoelectron momentum at the detector $\boldsymbol{k}_{t\to\infty}$ and the attoclock offset angle θ_A. The initial velocity along this direction v_{xi} in (12) is real. The classical velocity of the orbital motion $\boldsymbol{v}_{m=\pm1}$ adds up to the real velocity v_{xi} at the exit from the tunnel.

The angular maxima of $P_m(\theta)$ serve to determine the attoclock offset angle θ_A relative to the minor polarization axis of the laser pulse (the $\hat{x}$ axis in our coordinate frame, see Fig. 1 for illustration).

B. Analytical models

1. Semiclassical approach

We adopt the saddle-point method (SPM) [35] which relates the photoelectron momentum at the detector $\boldsymbol{k} \equiv \boldsymbol{k}_{t\to\infty}$ with a specific instant of tunneling t_i such that the semiclassical action along the photoelectron trajectory starting from this instant,

$$S_{\boldsymbol{k}}(t) = \int_{t_i}^{t} dt' \{[\boldsymbol{k} + A(t')]^2/2 + I_p\}, \tag{8}$$

is stationary:

$$\partial S_{\boldsymbol{k}}(t_i)/\partial t = [\boldsymbol{k} + \boldsymbol{A}(t_i)]^2/2 + I_p = 0. \tag{9}$$

In a general case, several solutions of Eq. (9) lead to the final photoelectron momentum $\boldsymbol{k}$ and the PMD is given by the sum over the corresponding tunneling ionization times [16]

$$P_m(\boldsymbol{k}) \propto \sum_{i=1}^{N_{\rm SP}} |\phi_{nlm}(\boldsymbol{v}_i)|^2 [S''_{\boldsymbol{k}}(t_i)]^{-1} \exp[iS_{\boldsymbol{k}}(t_i)]. \tag{10}$$

Here, the target orbital in the momentum space $\phi_{nlm}(\boldsymbol{v}_i)$ depends on the initial velocity at the instant of tunneling $\boldsymbol{v}_i = \boldsymbol{k} + \boldsymbol{A}(t_i)$. We note that for very intense fields I_p can be neglected in Eq. (9) and $\boldsymbol{v}_i = 0$.

For few-cycle circularly or elliptically polarized laser pulses, the number of the saddle points for a given momentum $N_{\rm SP} = N + 1$ [36]. For a continuous wave when $N \to \infty$, the solution of (9) can be found analytically [16,30,37]. In this case, the initial velocity

$$\boldsymbol{v}_i = \boldsymbol{k}_0 + A_0[\cosh(\omega\tau_0)\,\boldsymbol{e}_x + i\sinh(\omega\tau_0)\,\boldsymbol{e}_y]. \tag{11}$$

Here, $\omega\tau_0 = \sinh^{-1}\gamma$ and the Keldysh parameter $\gamma = \sqrt{2I_p}/A_0$. In Eq. (11), $k_0 = A_0\sinh(\omega\tau_0)/(\omega\tau_0)$ defines the peak position of the PMD. In the tunneling ionization regime, $\omega\tau_0 \simeq \gamma \lesssim 1$ and Eq. (11) can be reduced to

$$v_{xi} \simeq A_0\gamma^2/3, \quad v_{yi} \simeq iA_0\gamma = i\kappa. \tag{12}$$

The purely imaginary initial velocity v_{yi} is related to the linear momentum of the bound electron $\kappa = \sqrt{2I_p}$.

The target orbital factor in Eq. (10) brings in the angular momentum projection dependence

$$P_m(\boldsymbol{k}) \propto |\exp(im\phi_v)|^2, \quad \tan\phi_v = v_{yi}/v_{xi}. \tag{13}$$

In the case of an np target orbital, Eq. (11) leads to

$$\frac{P_{np_{-1}}(k_0)}{P_{np_{+1}}(k_0)} = \frac{|3+\gamma|^2}{|3-\gamma|^2} \simeq 1 + \frac{4\gamma}{3} \quad \text{as} \quad \gamma \to 0. \tag{14}$$

2. Classical considerations

The semiclassical action (8) and the SPM Eq. (9) do not differentiate the photoelectron trajectories with respect to the m projection. It is only the preexponential magnitude factor in Eq. (10) that makes the $m = \pm1$ ionization probabilities differ. Identical trajectories would mean the same angular profiles and the attoclock offset angle. However, various numerical simulations do not support this scenario. As was shown earlier [20,22] and will be demonstrated in the following, the offset angles in noble-gas atoms differ substantially and systematically for $m = \pm1$. In previous works [20,22], this difference was attributed to variation of the tunnel width and a stronger effect of the Coulomb field of the ion remainder when the photoelectron leaves the atom closer to the ionic core. To investigate this effect further, we employ here the following classical models.

a. Neglect of the Coulomb field. This model is expected to work in strong laser fields where the Coulomb field of the ion remainder can be neglected. We define the photoelectron trajectory in the laser field by the classical equations of motion

$$\boldsymbol{r}(t) = \int_{t_0}^{t} \boldsymbol{A}(\tau)d\tau + \boldsymbol{v}_f(t - t_0) + \boldsymbol{r}_0. \tag{15}$$

Here, $\boldsymbol{v}_f = \boldsymbol{v}_0 - \boldsymbol{A}(t_0)$ is the final velocity after the pulse end and $\boldsymbol{v}_0 = \boldsymbol{v}(t_0)$ is the initial velocity. The vector potential (3) is rewritten here as

$$\begin{aligned} A_x(t) &= -A_{x0}f(t)\cos\omega(t - t_0), \\ A_y(t) &= A_{y0}f(t)\sin\omega(t - t_0), \end{aligned} \tag{16}$$

where the envelope $f(t_0) = 1$, $f(t \to \infty) = 0$ and the magnitudes $A_{x0} = \epsilon A_0/\sqrt{1+\epsilon^2} < A_{y0} = A_0/\sqrt{1+\epsilon^2}$. The peak electric field at t_0 is directed along $\hat{y}$ and the photoelectron exit point $\boldsymbol{r}_0 = (0, y_0)$. We assume that $f(t)$ varies slowly. Under this assumption, the photoelectron trajectory (15) can

be expressed as

$$x(t) = -bf(t)\sin\omega(t-t_0) + v_f(t-t_0),$$
$$y(t) = -a[f(t)\cos\omega(t-t_0) - 1] + y_0, \tag{17}$$

where $a = A_{y0}/\omega$ and $b = A_{x0}/\omega$, $v_f = v_0 + A_{x0}$. After the pulse end, the trajectory becomes a straight line

$$x(t\to\infty) = v_f(t-t_0),$$
$$y(t\to\infty) = \xi a + y_0. \tag{18}$$

Here, we introduce a parameter ξ to account for a finite pulse duration. With an accuracy to $1/N^4$,

$$\xi = 1 + 1/N^2. \tag{19}$$

We relate the angular momentum projection of the bound electron m with its orbital velocity at the exit from the tunnel as shown schematically in Fig. 1. Thus, we augment the initial velocity after the tunneling v_{xi} given by Eq. (12) in the strong field limit, with this classical velocity:

$$v_0 = v_{xi} + m/y_0, \tag{20}$$

where the tunnel width

$$y_0 \simeq I_p/(\omega A_{y0}). \tag{21}$$

The initial momentum projection of the photoelectron at the exit from the tunnel

$$m_0 = v_0 y_0 = m + v_{xi} y_0 = m + M_0\gamma^2/3, \tag{22}$$

where

$$M_0 = A_{x0}y_0 \simeq \epsilon K_0, \quad K_0 = I_p/\omega, \tag{23}$$

and K_0 is the multiquantum parameter [38]. The final photoelectron angular momentum projection at the detector

$$M = v_f(\xi a + y_0)$$
$$= m + (1+\xi/3)M_0 + \left(1 + \frac{m}{M_0}\right)\frac{2\xi\mathcal{E}_0}{\epsilon\omega}. \tag{24}$$

Here, we introduced

$$\mathcal{E}_0 = \frac{A_{x0}^2}{2} = \frac{2\epsilon^2}{1+\epsilon^2}U_p, \quad U_p = A_0^2/4. \tag{25}$$

Similarly, the final photoelectron energy is

$$\mathcal{E} = \frac{(A_{x0}+v_0)^2}{2} \simeq \frac{\epsilon^2 I_p}{3} + \left(1 + \frac{2m}{M_0}\right)\mathcal{E}_0. \tag{26}$$

At large field intensities, $M \gg M_0 \gg m$. For long laser pulses $N \gg 1$ and $\xi \simeq 1$. Under these conditions, the photoelectron momentum projection gain can be expressed via the photoelectron energy at the detector:

$$\Delta M = M - m \simeq \frac{2\epsilon}{1+\epsilon^2}\frac{I_p + U_p + \mathcal{E}}{\omega}. \tag{27}$$

This expression relates the angular momentum projection gain of the photoelectron with the number of absorbed photons via the law of energy conservation.

b. Neglect of the laser field. For low-laser field intensity and short-pulse duration, the photoelectron trajectory is determined largely by the Coulomb field of the ion remainder. To determine such a trajectory, the classical Rutherford scattering model can be applied [28]. In this model, the distance of the closest approach in the Rutherford formula is equated with the tunnel width y_0 whereas the asymptotic electron velocity at infinity corresponds to the peak vector potential A_0. The resulting attoclock offset angle is expressed as

$$\tan\theta_{\rm KR} = \frac{\omega^2}{E_0^2}\frac{Z^*}{y_0} = \frac{1}{k_0^2}\frac{Z^*}{y_0}. \tag{28}$$

For neutral atomic targets, the asymptotic charge of the ion remainder $Z^* \simeq 1$. When this charge is fully screened, as in negative ions [39] or in the Yukawa potential [15], $Z^* \simeq 0$ and $\theta_A \to 0$. We will use this property of the KR model to conduct our further TDSE simulations in Sec. III D where we will reduce the asymptotic charge of the ion remainder to observe vanishing of the angular offset.

The dynamic factor in Eq. (28) can be rewritten as

$$\frac{1}{k^2 y_0} = \frac{\tau(k)F_{\rm max}}{k}, \quad F_{\rm max} = \frac{1}{y_0^2}, \quad \tau(k) = \frac{y_0}{k}. \tag{29}$$

Here, $F_{\rm max}$ is the maximum Coulomb force experienced by the electron at the exit from the tunnel and $\tau(k)$ is the time the photoelectron spends in the vicinity of the ion. In the KR model, which is applicable for short and weak laser pulses, y_0 is large and the photoelectron is accelerated to its final momentum k_0 while still interacting with the Coulomb field. Under the present conditions, the photoelectron is accelerated by the laser field even when it is far away from the laser field and hence $k < k_0$, which leads to $\tau = y_0/k > \tau_{\rm KR} = y_0/k_0$. Therefore, the actual attoclock offset angle is larger than prescribed by Eq. (28):

$$\tan\theta_A = C \times \tan\theta_{\rm KR}, \quad C = \frac{\tau_A}{\tau_{\rm KR}} > 1. \tag{30}$$

Thus, by comparing the numerical values of θ_A with predictions of Eq. (28), we can estimate the time the photoelectron interacts effectively with the Coulomb field.

III. RESULTS AND DISCUSSION

A. Numerical vs laboratory attoclock

The difference between the laboratory and numerical attoclocks with long and short pulses, respectively, is illustrated in Fig. 2. Here, the numerical attoclock results are exhibited in the top row of panels while analogous results for the laboratory attoclock are displayed in the bottom row. For illustrative purposes, we consider the Ar $3p$ photoionization by a single-cycle 2.9-fs pulse at 0.86×10^{14} W/cm^2 (top) and a multicycle 6.8-fs pulse at 3×10^{14} W/cm^2 (bottom).

The parametric plots in the left column represent the vector potential $\boldsymbol{A}(t)$ [Eq. (3)] with $N = 2$ (top) and $N = 7$ (bottom). Solutions of the SPM Eq. (9) corresponding to a given photoelectron momentum $\boldsymbol{k}$ can be visualized graphically by the intersects of $\boldsymbol{A}(t)$ with the straight line pointing in the $-\hat{\boldsymbol{k}}$ direction. Indeed, if I_p can be neglected in (9), then simply $\boldsymbol{k} = -\boldsymbol{A}(t_i)$. In a general case, three solutions can

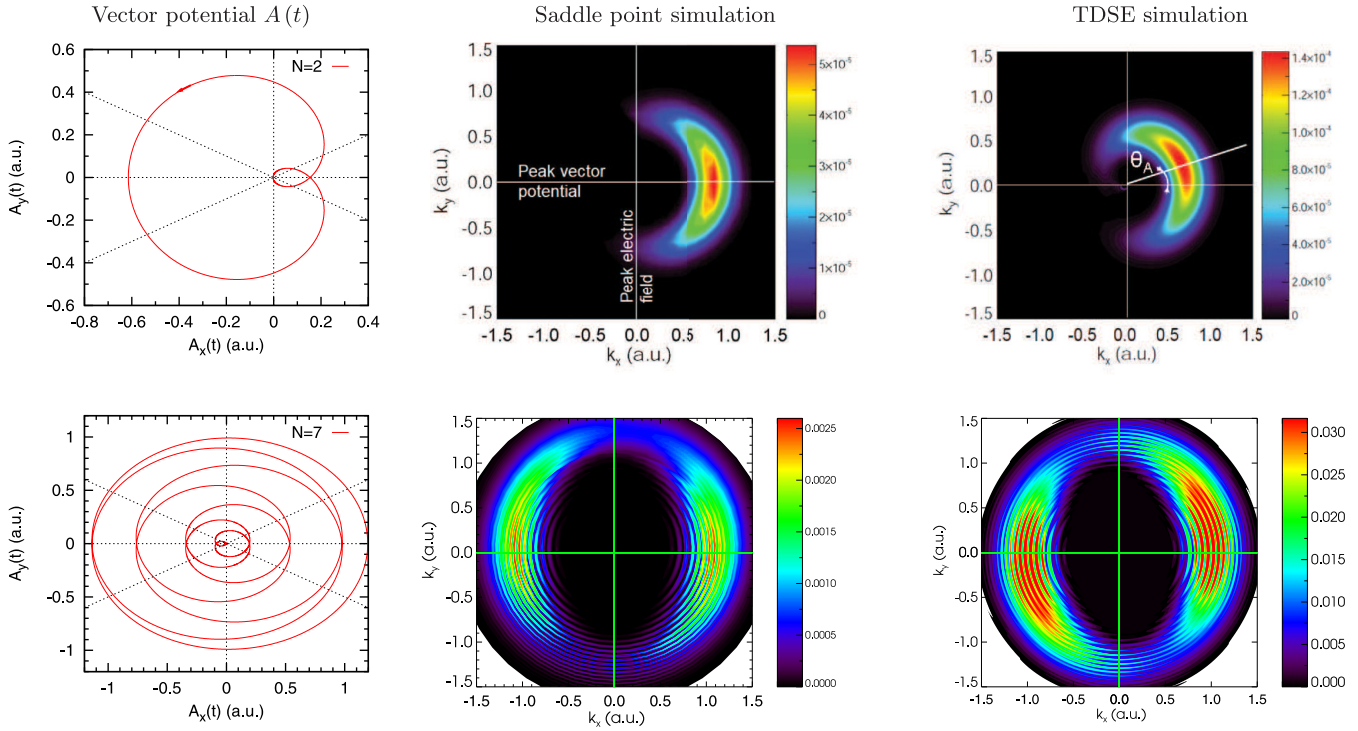

FIG. 2. From left to right: the parameteric plots of the vector potential $\boldsymbol{A}(t)$, the PMD (4) from the SPM simulations and that of the TDSE simulations. The top row of panels corresponds to the argon atom ionized with a nearly single-cycle 2.9-fs pulse at 0.86×10^{14} W/cm^2. The bottom row of panels visualizes the same ionization process driven by a multicycle 6.8-fs pulse at 3×10^{14} W/cm^2.

be identified for a short pulse with $N = 2$ of which two correspond to small values of $|A(t_i)|$ and do not contribute significantly to the PMD. The remaining "dominant" solution produces a well-formed lobe of intensity in the PMD graph shown in the top central panel. This image is obtained with an exponential accuracy visualizing the kinematic factor

$$\sum_{i}^{N_{\rm SP}} [S''_{\boldsymbol{k}}(t_i)]^{-1} \exp[iS_{\boldsymbol{k}}(t_i)],$$

while neglecting the squared momentum space orbital in the preexponential term. In the top right panel, we display a very similar PMD image returned by the TDSE calculation. The only visible difference between the top central and right panels is a rotation of the whole PMD by an attoclock offset angle θ_A. This rotation is entirely due to the Coulomb field which is neglected in the SPM.

The number of solutions in the case of a multicycle pulse is significantly greater. The eight solutions can be identified graphically in each of the positive and negative momentum directions. Accordingly, the PMD is symmetric in the $\pm k_x$ direction as is shown in the bottom central panel of Fig. 2. The ATI rings coming from the manifold of the SPM solutions are clearly visible in this panel. Again, as in the case of a short pulse visualized in the top row, the TDSE solution returns a very similar PMD image except for the angular rotation. Because of a number of ATI rings tilted differently, there is no single attoclock offset angle θ_A that can be easily identified to characterize the Coulomb field effect.

Further distinction between the numerical and laboratory attoclock is illustrated in Figs. 3 and 4 where we plot the corresponding photoelectron spectra (6) and their angular profiles (7), respectively. The energy spectra of the numerical and laboratory attoclock are shown in the top and bottom panels of Fig. 3, respectively. These spectra differ by the profound ATI structure on the former and its absence on the latter. Intensity varies dramatically between the magnetic projections, with $m = 0$ being strongly suppressed by the angular node of the target $3p$ orbital in the polarization plane. As to the other two projections, the ratio $P_{m=-1}/P_{m=1} \gg 1$ in line with Eq. (14). More detailed analysis of this ratio will be conducted in Sec. III B.

Equation (27) allows us to relate the photoelectron spectrum $P_m(E)$ with the angular momentum projection profile calculated as $P_m(M) \simeq \omega P_m(E)$. Except for very low photoelectron energy, the $P_m(E)$ and $P_m(M)$ profiles match each other rather well, both for the numeric (Fig. 3 top) and laboratory (Fig. 3 bottom) attoclocks.

The angular profiles of the numerical and laboratory attoclocks are displayed in the top and bottom panels of Fig. 4, respectively. While there is a single maximum in the angular profile of the numerical attoclock, there are two symmetric maxima in the case of the laboratory attoclock. Positions of the respected maxima are located by the Gaussian fitting illustrated in Fig. 4 for $m = -1$ profiles. Similar to the energy spectra, the angular profiles differ strongly in magnitude. The angular maxima positions are also displaced between various m projections.

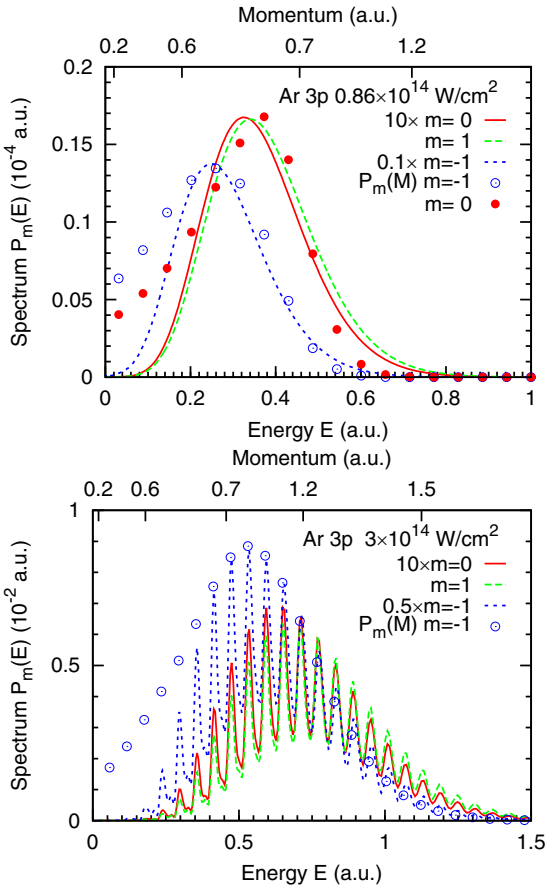

FIG. 3. Photoelectron spectrum, Eq. (6), of Ar $3p$ ionized with a single-cycle pulse at 0.86×10^{14} W/cm^2 (top) and a multicycle pulse at 3×10^{14} W/cm^2 (bottom). Various m spectra are scaled up and down relative to $m=1$ to fit the scale of the figure. The corresponding orbital momentum projection profiles $P_m(M)$ are converted to the photoelectron energy scale by Eq. (27) and overplotted.

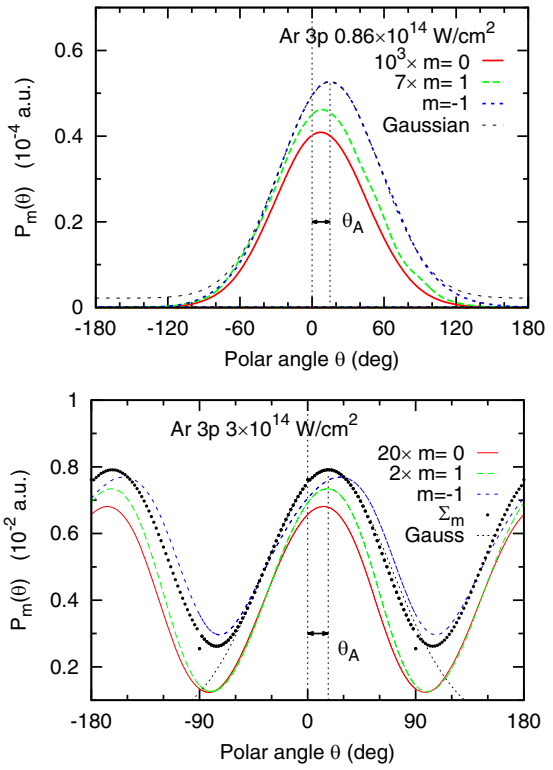

FIG. 4. Angular profiles (7) of the Ar $3p$ ionized with a single-cycle pulse at 0.86×10^{14} W/cm^2 (top) and a multicycle pulse at 3×10^{14} W/cm^2 (bottom). Various m profiles are scaled relative to $m=-1$ for better clarity. A Gaussian fit is used to locate positions of the corresponding angular maxima. The angular maxima of the $m=-1$ profiles are marked with the vertical dotted lines which define the corresponding attoclock offset angles θ_A. The bottom panel shows the PMD (4) integrated radially and marked as Σ_m.

B. Effect of the target orbital structure

In this section, we examine the target orbital structure effect on various observables returned by the TDSE calculations. As a case study, we consider the numerical attoclock on Ar $3p_m$ driven at $\lambda=800$ nm by a circularly polarized single-oscillation pulse. The field intensity range starts from a modestly nonadiabatic tunneling regime at $\gamma\simeq2$ and ends below the onset of the over-the-barrier ionization regime at $I_{\rm OBI}\simeq10^{15}$ W/cm^2 [40].

In the top panel of Fig. 5 we plot the most probable gain of the photoelectron momentum projection $\Delta M=M-m$ as obtained from the TDSE solution and as prescribed by Eq. (24). The latter equation predicts the linear increase of ΔM with the field intensity which is indeed the case. In the weak field regime, Eq. (24) is no longer valid and the numerical TDSE results deviate from the prescribed asymptotic limit $\Delta M=K_0(1+\xi/3)$. Both the numerical and analytical results for various m converge for low fields but deviate noticeably as the laser field grows. The gain ΔM is strongest for $m=1$ and the weakest for $m=-1$. This can be understood from the m-dependent term in Eq. (24) which appears due to the orbital velocity term m/y_0 in Eq. (20) under the assumption of the tunnel width y_0 being independent of m. Because the analytical predictions of Eq. (24) agree well with the numerical TDSE results for all m, it can suggest that the actual tunnel width is indeed independent of m, at least in the strong field regime.

In the middle panel of Fig. 5 we plot the mean photoelectron energy as returned by the TDSE calculations and compare it with the predictions of Eq. (26). As prescribed by this equation, the photoelectron energy grows linearly with the field intensity. At highest intensity, the analytical and numerical results agree well. In the low-field limit, the analytical results for all m values tend to $I_p/3$ while the numerical results fall below this value. In the bottom panel, we display the attoclock offset angles θ_A. Again, as in the case of the peak momentum values, the $m=-1$ projection is noticeably different from the two other m projections. When a comparison is made with the KR formula (28), the scaling factors $C=2$, 2.3, and 2.8 are deduced for $m=0$, 1, and -1, respectively. This correlates with predictions of a smaller initial velocity and hence a longer time (29) that the photoelectron interacts with the Coulomb field in the $m=-1$ case.

Equation (14) predicts the $m=\pm1$ ratio of the peak values of the PMD as determined by the semiclassical SPM expression (10) for a continuous wave. In Fig. 6 we compare Eq. (14) for Ar $3p$ with the TDSE and SPM results

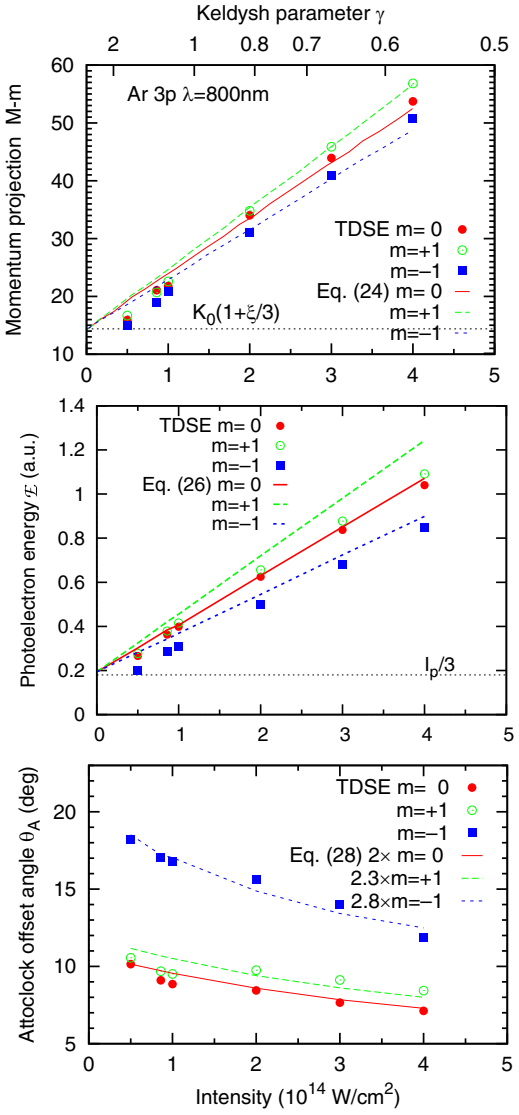

FIG. 5. Various observables returned by TDSE calculations on Ar $3p_m$ driven by a short circular pulse at 800 nm. Top: gain of the photoelectron momentum projection ΔM compared with Eq. (24). The low-field limit $\Delta M = K_0(1+\xi/3)$ is shown with the dotted line. Middle: mean photoelectron energy $\mathcal{E}$ is compared with Eq. (26). Bottom: the attoclock offset angle θ_A is compared with Eq. (28). The scaling factor C of Eq. (30) is shown for each m.

for a short pulse at $\lambda = 800$ nm. Both results agree with Eq. (14) even for larger Keldysh parameters $\gamma \simeq 1$ in a mildly nonadiabatic tunneling regime. At larger field intensities, the TDSE result approaches the $\gamma \to 0$ limit faster than the SPM result.

C. Comparison between various atoms

To make a comparison of the attoclock offset angles between various members of the noble-gas family, we take the experimentally measurable PMD (4) and subject it to a radial integration $\int k\,dk$. In doing so, we discard the m dependence which is not resolved experimentally. Such an angular profile is displayed in the bottom panel of Fig. 4 and marked as Σ_m along with the m-resolved angular profiles. Not surprisingly, the m-summed profile is very close to the dominant in magnitude $m = -1$ profile. Thus, obtained angular profiles are fitted with a Gaussian ansatz and the positions of their respective angular maxima are obtained. The displacement of these maxima relative to the minor polarization $\hat{x}$ axis gives the attoclock offset angles θ_A which are displayed in Fig. 7. The error bars shown in the figure result from a deviation of the angular profiles from a Gaussian shape noticeable in the bottom panel of Fig. 4. In the same Fig. 7 we display the offset angles for the numerical attoclock across a range of field intensities. To make a comparison with the laboratory attoclock, we select the dominant $m = -1$ projection. The angular profiles of the numerical attoclock have a perfect Gaussian shape, so the error bars are negligible here.

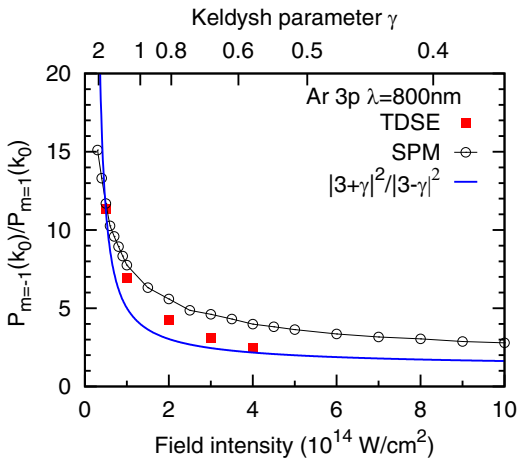

FIG. 6. Ratio of the peak PMD values for Ar $3p_{m=\pm1}$ is compared with the predictions of the semiclassical model (14).

The numerical attoclock offset angles become smaller as the ionization potential of the atom grows. This decrease of θ_A is in line with the prediction of the KR formula (28) and

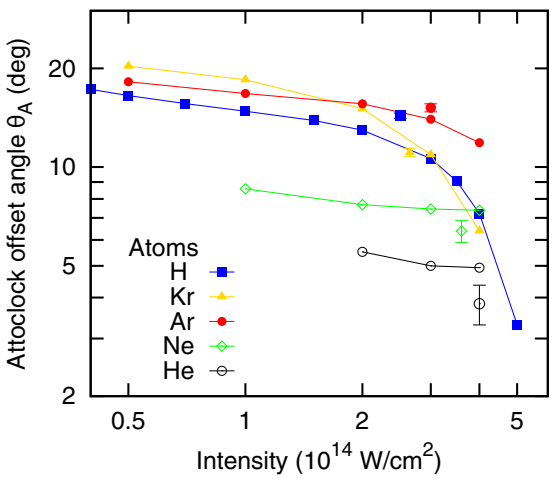

FIG. 7. Attoclock offset angles of various atoms versus driving pulse intensity. The numerical attoclock results with a short pulse are marked with colored lines. The laboratory attoclock values with a multicycle driving pulse at selected field intensities and $m = -1$ are shown with error bars of the matching plotting style.

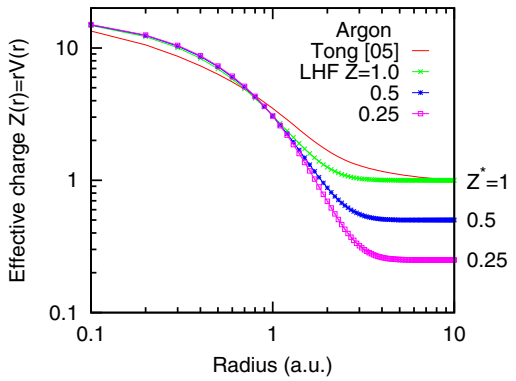

FIG. 8. Effective charge in Ar expressed via various one-electron potentials. The asymptotic values Z^* for various modifications of the localized Hartree-Fock potential are marked on the left vertical scale.

can be explained by the larger tunnel width $y_0 = I_p/E_0$. The hydrogen atom deviates somewhat from this tendency. This may be a subtle effect of its electronic structure which is different from the noble-gas atoms. A sharp decrease of θ_A for hydrogen towards the higher end of the field intensities reflects the onset of the over-the-barrier regime at $I_{\rm OBI} \simeq 0.5\times10^{14}$ W/cm^2 [40]. The laboratory attoclock offset angles are generally in line with their numerical counterparts.

D. Coulomb field effect

The KR expression (28) for the attoclock offset angle contains the asymptotic charge Z^* of the ion remainder. In this section, we treat this charge as an adjustable parameter. To do so, we modify the one-electron potential $V(r)$ entering the atomic Hamiltonian $\hat{H}_{\rm atom}$ and reduce Z^* gradually to zero. In this way, we aim to eliminate the Coulomb field effect on the attoclock offset angle. The effective charge can be expressed via the one-electron potential as $Z(r) = -rV(r)$ and the asymptotic value entering Eq. (28) is $Z^* = Z(r \to \infty)$.

In Fig. 8 we plot $Z(r)$ for various one-electron potentials used in our calculations for Ar. These are an empirical Tong [05] potential [41] and a localized Hartree-Fock (LHF) potential [42]. The latter potential has a simple analytical form

$$Z_{\rm HF}(r) = (Z_0 - Z^*)e^{-r/\lambda} + Z^*,$$

where Z_0 is the bare nucleus charge and λ is a screening length. In our simulations, we gradually decrease Z^* in several steps as shown in Fig. 8. At the same time, we adjust λ to maintain the binding energy of the $3p$ electron in Ar. The resulting PMDs projected onto the polarization plane (4) are exhibited in Fig. 9. The top panel should be compared with the top right panel of Fig. 2 where the empirical potential from [41] was used. As Z^* is gradually diminished, the offset angle is virtually reduced to zero at $Z^* = 0.25$. Interestingly, the ionization probability falls sharply when Z^* decreases. This is because the photoelectron becomes asymptotically free and can no longer absorb photons.

IV. CONCLUSIONS AND FURTHER DIRECTIONS

We have systematically studied tunneling ionization of noble-gas atoms with close to circularly polarized laser pulses

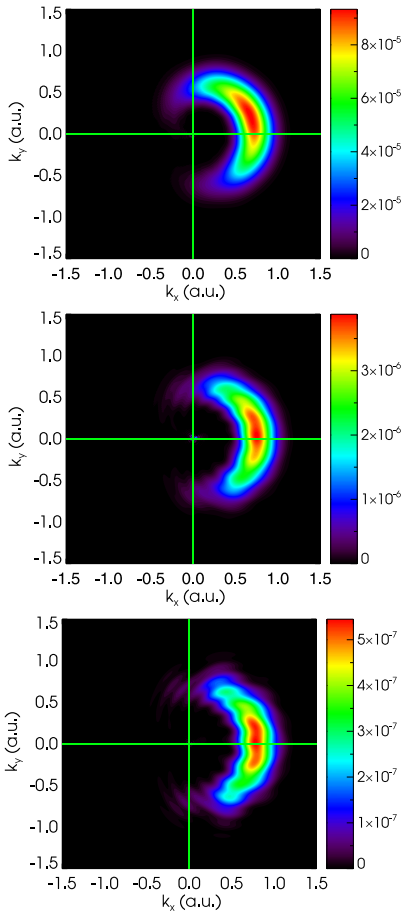

FIG. 9. The PMD (4) of Ar $3p$ driven by a single-cycle pulse at 0.86×10^{14} W/cm^2. The asymptotic charge of the ion remainder in the LHF potential is reduced from $Z^* = 1$ (top) to 0.5 (middle) and 0.25 (bottom).

in the attoclock field configuration. We simulated both the numerical and laboratory attoclocks driven by short, nearly single-cycle pulses and much longer multicycle pulses, respectively. Our numerical attoclock simulations covered a range of field intensities from a mildly nonadiabatic tunneling regime to the onset of over-the-barrier ionization. The laboratory attoclocks were simulated at selected energies while maintaining an approximately constant tunnel width.

We analyzed various observables generated from solutions of the time-dependent Schrödinger equation in the single active electron approximation. We also employed the semiclassical strong field ionization theory based on the saddle-point approximation, both in the analytical form for continuous waves and implemented numerically for short pulses. In addition, we developed a classical model tracing the photoelectron trajectory in the cases of strong and weak laser fields. In the former case, the Coulomb field of the ion reminder can be neglected while the latter condition allows to neglect the laser field.

We examined the most probable values of the photoelectron energy and the angular momentum projections as well as the attoclock offset angle. All these parameters demonstrate a strong dependence on the m projection of the initial bound state. This deviation is particularly strong for the attoclock

offset angles. In our field configuration, the $m = -1$ projection corresponds to the circularly polarized field counterrotating with the electron cloud in the initially bound state. Electrons with this m projection depart from the parent ion more slowly and are subjected much longer to its Coulomb field. Screening of this field reduces the attoclock offset angle virtually to zero. The tunneling width is found to be very similar for all the m projections and correlates well with the nominal tunnel width of the Keldysh theory of strong field ionization.

Our classical modeling makes quantitatively accurate predictions for the photoelectron energy and angular momentum projection gained from the laser field. The photoelectron energy spectrum is accessible directly from experiment while the angular momentum projection distribution can be easily obtained by virtue of the energy conservation. Both quantities can be compared with the analytical theory predictions thus providing a very direct way for calibrating experimental data.

The photoelectron energy at the detector depends linearly on the field intensity with the proportionality coefficient being dependent on the tunnel width. If the actual width dependence on the field intensity departs from the power law $I^{-1/2}$ prescribed by the Keldysh theory, then the linear scaling will be violated. If this power law is maintained but the proportionality with I_p is broken, this will be immediately reflected in the slope of the linear dependence of the photoelectron energy on the field intensity. Because the $m = -1$ component dominates strongly the measurable PMD, the experimental results can be compared directly with theoretical predictions thus testing the fundamental tunnel width expression of the Keldysh theory of strong field ionization.

These considerations give us hope that our numerical results and their theoretical interpretation will help to navigate the next generation of laboratory attoclock studies on noble-gas atoms. One set of these experiments is currently underway [23]. Recent progress of the nearly single-cycle optical pulse production with circular polarization [43] gives us hope that our simulations with numerical attoclock can also be experimentally verified.

ACKNOWLEDGMENTS

We gratefully acknowledge I. Litvinyuk, R. Sang, and S. Sainadh for many stimulating discussions. We thank S. Patchkovskii for placing his ISURF TDSE code at our disposal. A. Bray let us use his *Mathematica* script for SPM computations. Resources of National Computational Infrastructure facility (NCI Australia) have been employed.

[1] C. P. J. Martiny, M. Abu-samha, and L. B. Madsen, Ionization of oriented targets by intense circularly polarized laser pulses: Imprints of orbital angular nodes in the two-dimensional momentum distribution, Phys. Rev. A **81**, 063418 (2010).

[2] M. Abu-samha and L. B. Madsen, Alignment dependence of photoelectron momentum distributions of atomic and molecular targets probed by few-cycle circularly polarized laser pulses, Phys. Rev. A **94**, 023414 (2016).

[3] L. Arissian, C. Smeenk, F. Turner, C. Trallero, A. V. Sokolov, D. M. Villeneuve, A. Staudte, and P. B. Corkum, Direct Test of Laser Tunneling with Electron Momentum Imaging, Phys. Rev. Lett. **105**, 133002 (2010).

[4] I. A. Ivanov, A. S. Kheifets, J. E. Calvert, S. Goodall, X. Wang, H. Xu, A. J. Palmer, D. Kielpinski, I. V. Litvinyuk, and R. T. Sang, Transverse electron momentum distribution in tunneling and over the barrier ionization by laser pulses with varying ellipticity, Sci. Rep. **6**, 19002 (2016).

[5] P. Eckle, A. N. Pfeiffer, C. Cirelli, A. Staudte, R. Dorner, H. G. Muller, M. Buttiker, and U. Keller, Attosecond ionization and tunneling delay time measurements in helium, Science **322**, 1525 (2008).

[6] P. Eckle, M. Smolarski, P. Schlup, J. Biegert, A. Staudte, M. Schoffler, H. G. Muller, R. Dorner, and U. Keller, Attosecond angular streaking, Nat. Phys. **4**, 565 (2008).

[7] A. N. Pfeiffer, C. Cirelli, M. Smolarski, D. Dimitrovski, M. Abu-samha, L. B. Madsen, and U. Keller, Attoclock reveals natural coordinates of the laser-induced tunneling current flow in atoms, Nat. Phys. **8**, 76 (2012).

[8] M. Han, P. Ge, Y. Shao, Q. Gong, and Y. Liu, Attoclock Photoelectron Interferometry with Two-Color Corotating Circular Fields to Probe the Phase and the Amplitude of Emitting Wave Packets, Phys. Rev. Lett. **120**, 073202 (2018).

[9] M. Han, P. Ge, Y. Fang, X. Yu, Z. Guo, X. Ma, Y. Deng, Q. Gong, and Y. Liu, Unifying Tunneling Pictures of Strong-Field Ionization with an Improved Attoclock, Phys. Rev. Lett. **123**, 073201 (2019).

[10] R. Boge, C. Cirelli, A. S. Landsman, S. Heuser, A. Ludwig, J. Maurer, M. Weger, L. Gallmann, and U. Keller, Probing Nonadiabatic Effects in Strong-Field Tunnel Ionization, Phys. Rev. Lett. **111**, 103003 (2013).

[11] A. S. Landsman, M. Weger, J. Maurer, R. Boge, A. Ludwig, S. Heuser, C. Cirelli, L. Gallmann, and U. Keller, Ultrafast resolution of tunneling delay time, Optica **1**, 343 (2014).

[12] N. Camus, E. Yakaboylu, L. Fechner, M. Klaiber, M. Laux, Y. Mi, K. Z. Hatsagortsyan, T. Pfeifer, C. H. Keitel, and R. Moshammer, Experimental Evidence for Quantum Tunneling Time, Phys. Rev. Lett. **119**, 023201 (2017).

[13] C. Hofmann, A. S. Landsman, and U. Keller, Attoclock revisited on electron tunneling time, J. Mod. Opt. **66**, 1052 (2019).

[14] A. S. Kheifets, The attoclock and the tunneling time debate, J. Phys. B: At. Mol. Opt. Phys. **53**, 072001 (2020).

[15] U. S. Sainadh, H. Xu, X. Wang, A. Atia-Tul-Noor, W. C. Wallace, N. Douguet, A. Bray, I. Ivanov, K. Bartschat, A. Kheifets *et al.*, Attosecond angular streaking and tunneling time in atomic hydrogen, Nature (London) **568**, 75 (2019).

[16] I. Barth and O. Smirnova, Nonadiabatic tunneling in circularly polarized laser fields: Physical picture and calculations, Phys. Rev. A **84**, 063415 (2011).

[17] I. Barth and O. Smirnova, Spin-polarized electrons produced by strong-field ionization, Phys. Rev. A **88**, 013401 (2013).

[18] D. Trabert, A. Hartung, S. Eckart, F. Trinter, A. Kalinin, M. Schöffler, L. P. H. Schmidt, T. Jahnke, M. Kunitski, and R.

Dörner, Spin and Angular Momentum in Strong-Field Ionization, Phys. Rev. Lett. **120**, 043202 (2018).

[19] I. A. Ivanov and A. S. Kheifets, Time delay in atomic photoionization with circularly polarized light, Phys. Rev. A **87**, 033407 (2013).

[20] Y. Li, P. Lan, H. Xie, M. He, X. Zhu, Q. Zhang, and P. Lu, Nonadiabatic tunnel ionization in strong circularly polarized laser fields: Counterintuitive angular shifts in the photoelectron momentum distribution, Opt. Express **23**, 28801 (2015).

[21] J.-P. Wang and F. He, Tunneling ionization of neon atoms carrying different orbital angular momenta in strong laser fields, Phys. Rev. A **95**, 043420 (2017).

[22] Q. Zhang, G. Basnayake, A. Winney, Y. F. Lin, D. Debrah, S. K. Lee, and W. Li, Orbital-resolved nonadiabatic tunneling ionization, Phys. Rev. A **96**, 023422 (2017).

[23] S. Sainadh Undurti, R. Sang, and I. Litvinyuk (private communication).

[24] M.-H. Yuan and X.-B. Bian, Angular distribution of photoelectron momentum in above-threshold ionization by circularly polarized laser pulses, Phys. Rev. A **101**, 013412 (2020).

[25] L. Torlina, F. Morales, J. Kaushal, I. Ivanov, A. Kheifets, A. Zielinski, A. Scrinzi, H. G. Muller, S. Sukiasyan, M. Ivanov, *et al.*, Interpreting attoclock measurements of tunneling times, Nat. Phys. **11**, 503 (2015).

[26] H. Ni, U. Saalmann, and J.-M. Rost, Tunneling Ionization Time Resolved by Backpropagation, Phys. Rev. Lett. **117**, 023002 (2016).

[27] J. Liu, Y. Fu, W. Chen, Z. Lü, J. Zhao, J. Yuan, and Z. Zhao, Offset angles of photocurrents generated in few-cycle circularly polarized laser fields, J. Phys. B: At. Mol. Opt. Phys. **50**, 055602 (2017).

[28] A. W. Bray, S. Eckart, and A. S. Kheifets, Keldysh-Rutherford Model for the Attoclock, Phys. Rev. Lett. **121**, 123201 (2018).

[29] V. V. Serov, A. W. Bray, and A. S. Kheifets, Numerical attoclock on atomic and molecular hydrogen, Phys. Rev. A **99**, 063428 (2019).

[30] A. Perelomov, V. Popov, and M. Terent'ev, Ionization of atoms in an alternating electric field II, J. Exptl. Theoret. Phys. **50**, 1393 (1966) [Sov. Phys. JETP **24**, 207 (1967)].

[31] S. Patchkovskii and H. Muller, Simple, accurate, and efficient implementation of 1-electron atomic time-dependent schrödinger equation in spherical coordinates, Comput. Phys. Commun. **199**, 153 (2016).

[32] V. V. Serov, Calculation of intermediate-energy electron-impact ionization of molecular hydrogen and nitrogen using the paraxial approximation, Phys. Rev. A **84**, 062701 (2011).

[33] F. Morales, T. Bredtmann, and S. Patchkovskii, iSURF: A family of infinite-time surface flux methods, J. Phys. B: At. Mol. Opt. Phys. **49**, 245001 (2016).

[34] V. V. Serov, V. L. Derbov, T. A. Sergeeva, and S. I. Vinitsky, Hybrid surface-flux method for extraction of the ionization amplitude from the calculated wave function, Phys. Rev. A **88**, 043403 (2013).

[35] M. Ivanov, in *Ionization in Strong Low-Frequency Fields, Attosecond and XUV Spectroscopy: Ultrafast Dynamics and Spectroscopy*, 1st ed. (Wiley, Weinheim, 2014), pp. 179–200.

[36] D. B. Milošević, G. G. Paulus, D. Bauer, and W. Becker, Above-threshold ionization by few-cycle pulses, J. Phys. B: At. Mol. Opt. Phys. **39**, R203 (2006).

[37] V. D. Mur, S. V. Popruzhenko, and V. S. Popov, Energy and momentum spectra of photoelectrons under conditions of ionization by strong laser radiation (the case of elliptic polarization), J. Exptl. Theoret. Phys. **119**, 893 (2001) [Sov. Phys. JETP **92**, 777 (2001)].

[38] S. V. Popruzhenko, Keldysh theory of strong field ionization: history, applications, difficulties and perspectives, J. Phys. B: At. Mol. Opt. Phys. **47**, 204001 (2014).

[39] N. Douguet and K. Bartschat, Attoclock setup with negative ions: A possibility for experimental validation, Phys. Rev. A **99**, 023417 (2019).

[40] Toru Morishita, Keldysh parameter calculator (2020), http://power1.pc.uec.ac.jp/~toru/keldysh/

[41] X. M. Tong and C. D. Lin, Empirical formula for static field ionization rates of atoms and molecules by lasers in the barrier-suppression regime, J. Phys. B: At. Mol. Opt. Phys. **38**, 2593 (2005).

[42] A. W. Bray, F. Naseem, and A. S. Kheifets, Simulation of angular-resolved RABBITT measurements in noble-gas atoms, Phys. Rev. A **97**, 063404 (2018).

[43] M. Ouillé, A. Vernier, F. Böhle, M. Bocoum, A. Jullien, M. Lozano, J.-P. Rousseau, Z. Cheng, D. Gustas, A. Blumenstein, P. Simon, S. Haessler, J. Faure, T. Nagy, and R. Lopez-Martens, Relativistic-intensity near-single-cycle light waveforms at kHz repetition rate, Light: Sci. Appl. **9**, 47 (2020).